PAPER

Preparation of TiO₂/porous glass-H with the coupling of photocatalysis oxidation–adsorption system in the initial position and its desulfurization performance on model fuel†

Yue Liu, [ID] Jing-zhi Tian,* Xin Hao, Yong-jie Zheng, Tao Jing, Yun-peng Zhao and Wan-li Yang

TiO₂/porous glass-H as composite catalysts were synthesized hydrothermally in the presence of H_2O_2 using porous glass microspheres as carriers. The photocatalytic-adsorptive desulfurization of model fuel by composite catalysts was investigated under UV irradiation. The structure and morphology of the composite catalysts were characterized *via* scanning electron microscopy (SEM), N_2 adsorption, X-ray diffraction (XRD) and ultraviolet-visible spectroscopy (UV-vis). The results showed that TiO₂/porous glass-H exhibited a significantly enhanced photocatalytic-adsorption desulfurization performance due to its enhanced surface area, highly enhanced light absorption, and reduced recombination of photogenerated electron pairs compared with TiO₂/porous glass synthesized in the absence of H_2O_2. The optimized TiO₂ loading was 20% and the reaction temperature was 303.15 K, which could achieve almost 100% sulfur removal when 0.1 g catalyst was applied to a sulfide concentration of 300 mg L⁻¹. Based on the kinetic fitting of the obtained data, it was found that the rate-controlling step of sulfide adsorption on the catalyst was a molecular diffusion process and the adsorption intensity and adsorption capacity of the composite catalyst were significantly improved compared with the porous glass-H in the adsorption thermodynamic curve, and ΔS, ΔH and ΔG of the adsorption process were calculated. In addition, TiO₂/porous glass-H could be regenerated *via* simple heat treatment, exhibiting similar efficiency as the original TiO₂/porous glass-H after three regeneration cycles.

1 Introduction

Many species of organosulfur compounds remaining in petroleum products such as diesel, gasoline and jet fuel will release a large amount of sulfur oxides after combustion. The accumulation of sulfur oxides in air is one of the main causes of global warming, acid rain and air pollution. Thus, ultra-clean fuel has attracted widespread attention worldwide.[1–3]

Currently, desulfurization technologies mainly include two categories, hydrodesulfurization (HDS) technology and non-hydrodesulfurization (non-HDS) technology.[4,5] The industrialized HDS process is usually operated at high temperature and high pressure, which is effective for the removal of acyclic and aliphatic sulfides, but inefficient for the removal of thiophene and its derivatives, given that they require higher hydrogen and energy consumption and higher octane loss values due to steric hindrance effects.[6–8] Therefore, the development of non-HDS

technology with low energy consumption and mild reaction conditions is highly significant. Non-HDS technology is categorized as extractive desulfurization,[9] adsorption desulfurization (ADS),[10,11] oxidative desulfurization[12–14] and microbial desulfurization[15,16]

The ADS process is performed under ambient conditions and is considered an efficient method for producing fuels. It can be a pretreatment step for the HDS process and provides an alternative method for the treatment of an extremely low sulfur content.[17] The strong competitive adsorption of coexisting aromatic compounds, such as polyaromatic hydrocarbons and nitrogen compounds, cannot be ignored for ultra-deep desulfurization of real fuels, although significant progress has been made in the development of new adsorbents for the ADS process.[18,19] To improve the adsorption selectivity of ADS and expand its potential applications, different methods have been carried out to functionalize the adsorption materials.[20,21] The coupled photocatalytic oxidation–adsorption process is a promising method, by which organosulfur compounds are photocatalytically oxidized to form polar sulfoxides or sulfones over a catalyst or adsorbent in the initial step, which are then selectively adsorbed on photocatalytic oxidation–adsorption

College of Chemistry and Chemical Engineering, Qiqihar University, Qiqihar, Heilongjiang 161000, China. E-mail: zwlwtg1234@163.com

† Electronic supplementary information (ESI) available. See DOI: 10.1039/d1ra04466d

bifunctional materials.[22–24] TiO$_2$-based metal oxides have been widely used in the coupled photocatalytic-adsorptive desulfurization process due to the advantage of high photocatalytic ability, low cost and stable properties.[25,26] Amin *et al.*[27] investigated a photocatalytic-adsorptive system using high-performance microporous titania–silica (TiO$_2$–SiO$_2$) nanocomposites for the ultra-deep desulfurization of dibenzothiophene (DBT). The selective mechanism was demonstrated, where DBT is first oxidized to dibenzothiophene sulfone (DBTO$_2$) with higher polarity, which is subsequently adsorbed on TiO$_2$–SiO$_2$. Ren *et al.*[28] reported a coupling photocatalytic oxidation–adsorption (CADS) system for diesel using ultrasonic-assisted wet impregnation to load TiO$_2$ on an SBA-15 carrier for ultra-deep DBT adsorption, and found that both the saturated adsorption capacity of dibenzothiophene and adsorption equilibrium constant increased by 20 times compared with the pure adsorbent (ADS) without oxidant. Li *et al.*[29] synthesized TiO$_2$ on an SiO$_2$ carrier using the hydrothermal method. To study the influence of aromatics in diesel on the photocatalytic adsorption desulfurization performance of Ti$_x$SiO$_y$-H, model fuels with different contents of toluene were used for the desulfurization experiments. The sulfur removal rate dropped sharply from 43.1% to zero when the toluene content increased from zero to 25 wt% if no ultraviolet light irradiation was applied. On the contrary, the sulfur removal rate in the same model fuel approached 98.4% after 5 h ultraviolet radiation. Previous work demonstrated that the coupling of photocatalytic-adsorption catalysts *via* the *in situ* conversion of thiophenic compounds into sulfones over an adsorbent can effectively inhibit competitive adsorption and increase the adsorption efficiency of sulfur, which is a promising approach to improve the adsorption selectivity of ultra-deep desulfurization.[30–32]

In this work, a portable coupled photocatalytic oxidation–adsorption process under mild conditions using TiO$_2$/porous glass-H as a composite catalyst was systematically investigated. Porous glass was prepared *via* a simple high-temperature and high-pressure etching method, and the hydrothermal method was used to load TiO$_2$ on the porous glass carriers. The composite catalyst was characterized *via* N$_2$-adsorption, XRD and UV-vis spectroscopy. The desulfurization performance of various catalysts prepared under different conditions were measured in a batch photochemical reactor and the effect of TiO$_2$ loading was optimized. The kinetics of TiO$_2$-H, TiO$_2$/porous glass-H and porous glass-H were investigated and modeled. Moreover, the Langmuir isotherm model was used to fit the TiO$_2$/porous glass-H desulfurization data and compared with the isotherm of the carriers without the *in situ* catalytic reaction. The effects of the initial concentration of sulfide in the model fuels and the adsorption temperature on the saturated adsorption capacity were explored. Finally, the recyclability of TiO$_2$/porous glass-H was investigated.

2 Experimental

2.1 Reagents and instruments

Solid glass microspheres (70–110 μm) were supplied by Suzhou Chengen Chemical Co., Ltd., China. Dibenzothiophene (DBT, 99%) and octane (96%) were obtained from Shanghai Maclean Biochemical Technology Co., Ltd., China. Isopropanol (99.7%), hydrogen peroxide (H$_2$O$_2$, 30%) and acetone (99.5%) were supplied by Tianjin Kaitong Chemical Reagent Co., Ltd., China. Tetrabutyl titanate (TNBT, 98%) and hexadecyltrimethylammonium bromide (CTAB, 99%) were obtained from Tianjin Kemiou Chemical Reagent Co., Ltd., China.

The collector magnetic stirrer (DF-II) was produced by Jiangsu Jintan Ronghua Instrument Manufacturing Co., Ltd., China; the high temperature and high pressure reactor (YZRJ-250) was produced by Shanghai Yanzheng Experimental Instrument Co., Ltd., China; the vacuum drying oven (DZF-6020) was produced by Shanghai Heng Technology Co., Ltd., China; the muffle furnace (FO310C) was produced by Yama Technology Co., Ltd., Japan; the photocatalytic instrument (BL-GHX-V) was produced by Shanghai Biran Instrument Co., Ltd., China; the X-ray diffractometer (D8-Focus) was produced by Bruker, Germany; the scanning electron microscope (H-7650) was produced by Hitachi Co., Ltd., Japan; the specific surface area pore size distribution analyzer (NOVA 1200e) was produced by Kantar Instruments; and the three tandem quadrupole mass spectrometer (7890b-7000c) was produced by Agilent Company, United States.

2.2 Photocatalyst/adsorbent synthesis

2.2.1 Preparation of porous glass carrier. Porous glass microsphere carriers were synthesized using a high-temperature and high-pressure etching method. Briefly, 5.0 g glass microspheres and 200 mL water were placed in a pressure reactor. Subsequently, the pressure of the reactor was gradually increased to 12.5 MPa, and the temperature was maintained at 325 °C for 2 h. The porous glass microspheres were then separated from the water by filtration and washed with deionized water several times to pH = 7, followed by drying in an oven at 80 °C for 4 h.

2.2.2 Preparation of TiO$_2$/porous glass-H. TiO$_2$/porous glass-H with various TiO$_2$ loadings (x = 0, 5 wt%, 10 wt%, 15 wt%, 20 wt% and 25 wt%) and TiO$_2$-H were synthesized *via* the hydrothermal method. In a typical synthesis procedure, 0.7 mL tetrabutyl titanate (TNBT) was added to a mixed solution of 13 mL hydrogen peroxide and 20 mL isopropanol, where the obtained solution was transparent and yellow colored, and then 0.03 g CTAB and 0.65 g porous glass carriers were thoroughly mixed with the above mixed solution, which was denoted as solution A. Then, 5 mL water and 10 mL isopropanol were mixed, which was denoted as solution B. Subsequently, solution B was added to solution A dropwise under stirring at 30 °C for 0.5 h. After TNBT was hydrolyzing at 50 °C for 1 h, the resulting mixture was then transferred to a stainless steel autoclave for crystallization at 140 °C for 4 h. After that, the obtained precipitate was filtered, washed with distilled water, dried at 80 °C, and then calcined at 450 °C in air for 3 h.

The conventional TiO$_2$/porous glass, porous glass-H and TiO$_2$-H were synthesized following the same procedure, as described above, but without the addition of H$_2$O$_2$, TNBT and porous glass carrier to solution A, respectively.

2.3 Desulfurization experiments

Desulfurization experiments with/without UV irradiation were conducted in a photochemical reactor. The reaction system consisted of a 500 W xenon lamp as the light source, a six 50 mL quartz tube reactors, a magnetic stirrer, and a circulator bath to control the temperature. Considering that all the reactions in our work were carried out at 20 °C, the overall evaporation loss of the model fuels and organosulfur compounds during the reaction was measured to be negligible.

The model fuels were prepared by dissolving given amounts of dibenzothiophene in octane. In a typical photocatalytic oxidation desulfurization experiment, 0.1 g of the photocatalyst/adsorbent and 50 mL of model fuel were added to a quartz test tube. After stirring vigorously in the dark for 1 h to attain adsorption–desorption equilibrium, the mixture was then irradiated by UV light for 4.5 h and the samples were taken every 0.5 h during the reaction. To make the analysis data accurate, the spent TiO_2/porous glass-H after the reaction was quickly separated by centrifugation.

2.4 Adsorption experiments

To investigate the isotherm of the photocatalyst/adsorbent and the carrier, 0.1 g of the prepared adsorbent was put into 50 mL of aqueous solution with various initial concentrations of dibenzothiophene (DBT). The mixture was stirred at 150 rpm for 4 h at a temperature of 303.15 K. Samples were taken out every 30 min to measure the DBT concentration using the method described in Section 2.2.

To investigate the adsorption kinetics, 0.1 g of each photocatalyst, photocatalyst/adsorbent and carrier was added to 50 mL model fuel with 300 mg L^{-1} sulfide. Samples were taken out periodically to measure the DBT concentration in the same manner as described above.

2.5 Configuration of standard samples and analysis of the treated fuel samples

Firstly, 0.9 g DBT was dissolved in 1 L *n*-octane to prepare a batch solution with a concentration of 900 ml L^{-1}. Subsequently, the batch solution was diluted with varying amounts of *n*-octane to make DBT/*n*-octane solution with a concentration of 900 mg L^{-1}, 700 mg L^{-1}, 500 mg L^{-1}, 400 mg L^{-1}, 300 mg L^{-1}, 200 mg L^{-1}, 100 mg L^{-1} and 50 mg L^{-1}.

The concentration of sulfur was detected on a triple quadrupole gas-mass spectrometer (Agilent GC/MS-MS, 7890b-7000c). The GC was equipped with a DB-1 quartz capillary column (0.25 μm × 0.25 mm × 30 m), and highly purified nitrogen (≥99.9995 wt%) was used as the carrier gas. The chromatographic conditions are as follows: injection port temperature was 250 °C; injection volume was 1.0 μL; split ratio was 10; carrier gas flow rate was 1 mL min^{-1}; and oven temperature was kept at 60 °C for 2 min, and then increased to 230 °C at a heating rate of 5 °C min^{-1}, and held at 230 °C for 2 min. The mass spectrometry conditions are described as follows: ion source temperature was 220 °C; electron energy was 70 eV; detector voltage was 1.8 kV; scanning range was 40–550

μm; scanning interval was 0.5 s; and scanning rate was 500 μ s^{-1}. The sulfur removal efficiency was calculated according to the following equation:

$$x = \frac{C_0 - C_i}{C_0} \times 100\% \tag{1}$$

where x is the percentage of sulfur removed; C_0 is the initial concentration of sulfide in the model fuels and C_i is the sulfide concentration in the model fuels after desulfurization.

2.6 Regeneration of TiO_2/porous glass-H

In the regeneration process, the used TiO_2/porous glass-H adsorbent was filtered and washed three times with acetone to remove the adsorbed oxidized sulfur species. Subsequently, the washed photocatalyst/adsorbent was dried and calcined at 450 °C for 3 h. After that, the sample was used in the next desulfurization cycle.

2.7 Characterization

2.7.1 SEM. A small amount of sample powder was sprayed onto a conductive tape, and then gold was sprayed on to the sample surface. The morphology and dispersion of the catalyst were analyzed by SEM (H-7650, Japan) at an accelerating voltage of 15–20 kV.

2.7.2 N_2 adsorption–desorption measurement. Nitrogen adsorption–desorption isotherms were measured at 77 K on a Quantachrome NOVA 1200e chemisorption–physisorption analyzer. The samples were degassed under vacuum at 250 °C before testing. The specific surface area was calculated from the adsorption isotherms using the Brunauer–Emmett–Teller (BET) equation. The pore size distribution and total pore volume of the sample were evaluated from the desorption curve according to the Barrett–Joyner–Halenda (BJH) model.

2.7.3 XRD. The crystal structure of the sample was analyzed using a powder crystal X-ray diffractometer (D8-Focus, Bruker) with Cu Kα radiation ($\lambda = 1.54056$ nm) operated at 40 mA and 40 kV at a scanning rate of 4° min^{-1} from 10° to 80°.

2.7.4 UV-vis spectroscopy. The ultraviolet-visible spectra of the samples were recorded on a UV-vis spectrometer (UV-2450, Shimadzu) in the range of 200–800 nm.

3 Results and discussion

3.1 Characterization

3.1.1 SEM measurement. Fig. 1(a–c) show the morphology of the raw glass microspheres, which possess a smooth and solid surface with small speckles (SEM pictures of different TiO_2 loadings are displayed in the ESI†). Fig. 1(d–f) show the surface morphology of the prepared porous glass beads, which present a fibrous structure with closed pores, and the diameters of the fibers are 0.18 (±0.055) μm and the average diameter of the porous glass microspheres is 125.0 (±8.36) μm, which are similar to that of the raw glass microspheres. Fig. 1(g–i) and (j–l) show the surface morphologies of the TiO_2/porous glass and TiO_2/porous glass-H synthesized in the absence and presence of H_2O_2, respectively. It can be seen that the TiO_2/porous glass
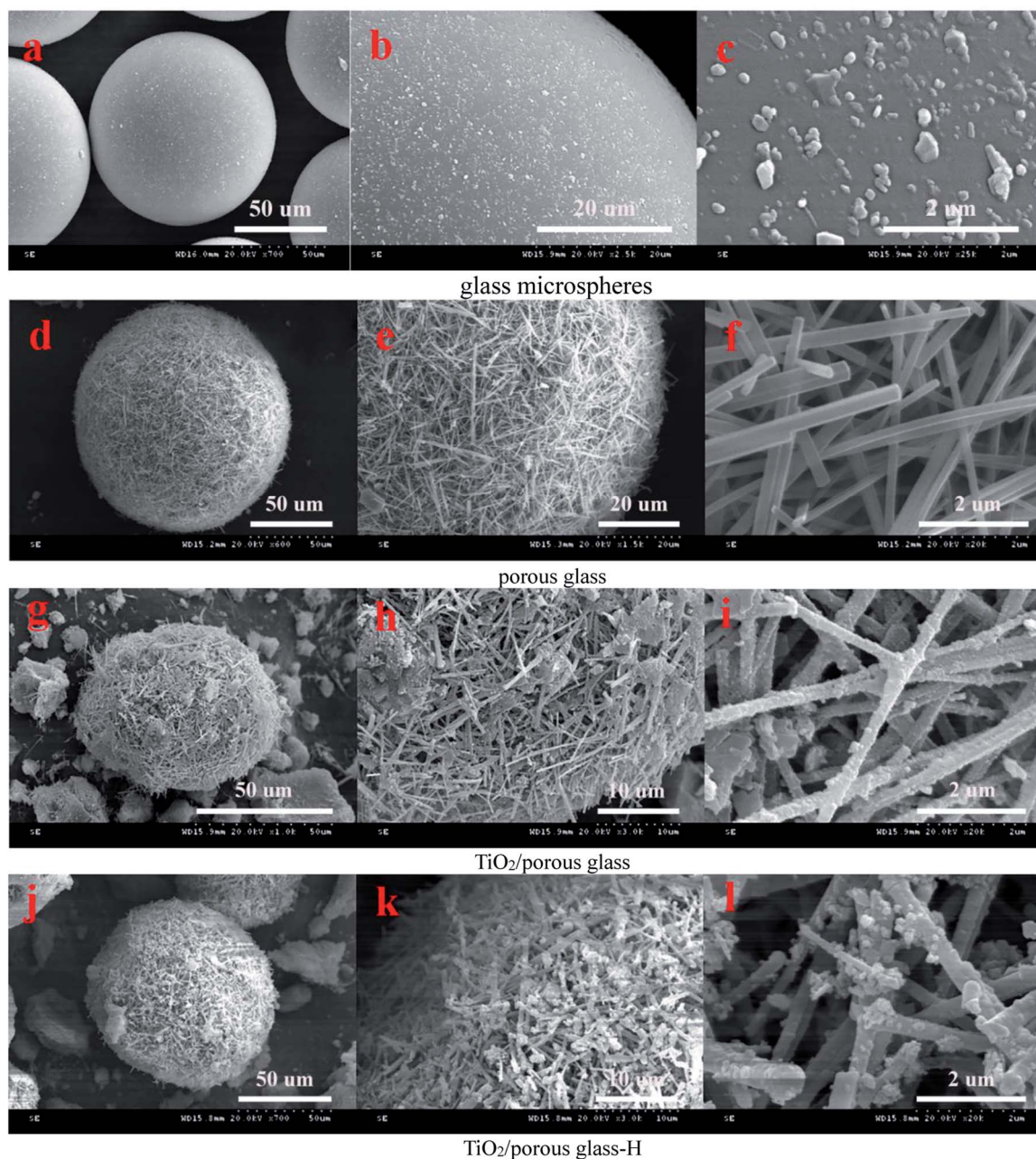
Fig. 1 SEM micrographs of glass beads (a–c), porous glass (d–f), TiO$_2$/porous glass (g–i) and TiO$_2$/porous glass-H (j–l).

Table 1 The textural properties of TiO$_2$-H, porous glass-H, TiO$_2$/porous glass and various TiO$_2$/porous glass-H materials

Catalyst	BET surface area (m^2 g^{-1})	Average pore size (nm)	Total pore volume (m^3 g^{-1})
Porous glass-H	157.979	9.613	0.224
TiO$_2$/porous glass	172.573	3.661	0.264
TiO$_2$/porous glass-H (x = 5 wt%)	186.184	4.228	0.334
TiO$_2$/porous glass-H (x = 10 wt%)	259.033	4.203	0.266
TiO$_2$/porous glass-H (x = 15 wt%)	299.127	3.626	0.276
TiO$_2$/porous glass-H (x = 20 wt%)	242.029	3.667	0.220
TiO$_2$/porous glass-H (x = 25 wt%)	216.766	3.866	0.303
TiO$_2$-H	90.415	18.316	0.173

exhibits both a fibrous structure and nano-spherical particles adhered on the fiber surfaces. As shown in Fig. 1(g) and (h), large-aggregated TiO_2 clusters can be observed on the TiO_2/porous glass, while more uniformly distributed TiO_2 can be observed on the fiber surfaces in TiO_2/porous glass-H synthesized in the presence of H_2O_2. Therefore, it can be speculated that the surface area of TiO_2/porous glass-H in the presence of H_2O_2 is larger than that of the TiO_2/porous glass under the same preparation conditions, which is consistent with the BET data presented in Table 1. The surface area of the TiO_2/porous glass is 172.57 m^2 g^{-1} and the surface area of the other TiO_2-supported TiO_2/porous glass-H catalysts is larger than that of the TiO_2/porous glass catalyst. The observation that TNBT is very easily hydrolyzed to form hydroxide precipitate in the presence of excess water has been reported in previous works.[33,34] However, some studies found that no precipitation was generated when TNBT was added to a mixture of isopropanol and 30% hydrogen peroxide aqueous solution. It can be speculated that the hydrolysis of TNBT may slow down in the presence of H_2O_2, which may be due to the strong interaction between Ti species and H_2O_2.[29,35,36] Therefore, the significant reduction in particle size and the larger BET surface area in TiO_2/porous glass-H can be ascribed to the slow hydrolysis of TNBT in the presence of H_2O_2.

3.1.2 XRD analysis.
Fig. 2 shows the XRD curves of TiO_2-H, porous glass-H and TiO_2/porous glass-H with varying TiO_2 loadings. It can be seen from Fig. 2 that there is no clear crystalline peaks on porous glass-H, indicating that porous glass-H is amorphous. The characteristic peaks at 25.44°, 37.84°, 47.99°, 53.95°, 62.95° and 75.34° are attributed to TiO_2-H single oxide, which corresponds to the (101), (103), (200), (105), (213), and (107) diffraction planes of the anatase phase, respectively[37–39] (ICDD 00-001-0562). No clear characteristic peaks of either the rutile or anatase phases of crystalline TiO_2 are observed in TiO_2/porous glass-H with 5 wt% TiO_2, which may be because TiO_2 is highly dispersed on the porous glass with smaller crystalline sizes beyond the detection limit of XRD. When the loading of

TiO_2 exceeded 5 wt%, strong characteristic peaks were observed at 25.44°, 37.84°, 47.99° and 53.95°, which are attributed to the crystals of TiO_2 in the anatase phase. Simultaneously, the intensity of the characteristic peaks gradually increased with an increase in the TiO_2 loading.

3.1.3 N_2 adsorption–desorption measurement.
Table 1 lists the textural properties of TiO_2-H, porous glass-H and TiO_2/porous glass-H with varying TiO_2 loadings and TiO_2/porous glass synthesized in the absence of H_2O_2. It can be observed that the BET surface area of TiO_2/porous glass-H first increased and then decreased with an increase in TiO_2 loading, and the inflection point appeared at a TiO_2 loading of 15 wt%. As previously reported in the literature, the coupling of polycrystals may result in an increase in surface area such as TiO_2 with MO_2 (M = Zr, Ce, and Si), given that the individual crystallization would have an inhibitory effect during the preparation process.[40–43] Therefore, the increase in the BET surface area with an increase in the TiO_2 loading up to 15 wt% may be caused by the inhibition of the individual crystallization and decrease in crystalline size. On the contrary, when the TiO_2 loading was greater than 15 wt%, the decrease in the surface area may be attributed to the increase in the crystalline size of TiO_2, as shown in the XRD curves in Fig. 2. Compared with porous glass-H, TiO_2/porous glass showed a much higher BET surface area and smaller pore size.

3.1.4 UV-vis spectrometric analysis.
Fig. 3 presents the UV-vis spectra of TiO_2-H, porous glass-H, TiO_2/porous glass and TiO_2/porous glass-H. It can be seen that TiO_2-H, TiO_2/porous glass and TiO_2/porous glass-H present strong absorption in the range of 200 to 400 nm, with a peak at around 300 nm. Compared with TiO_2/porous glass, the intensity of the absorption peak of TiO_2/porous glass-H is higher, suggesting that the surface area of the composite catalyst is larger and the rate of electron–hole pair formation increases when H_2O_2 is present during the preparation, resulting in enhanced photocatalytic activity. The forbidden band width corresponding to the
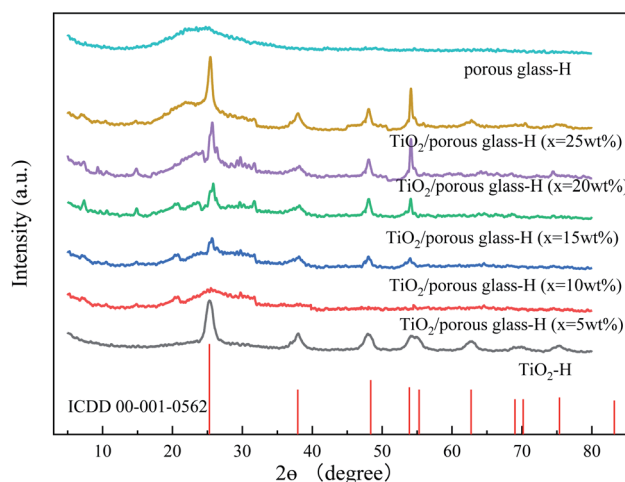

Fig. 2 XRD patterns of TiO_2-H, porous glass-H and TiO_2/porous glass-H with different TiO_2 loadings.
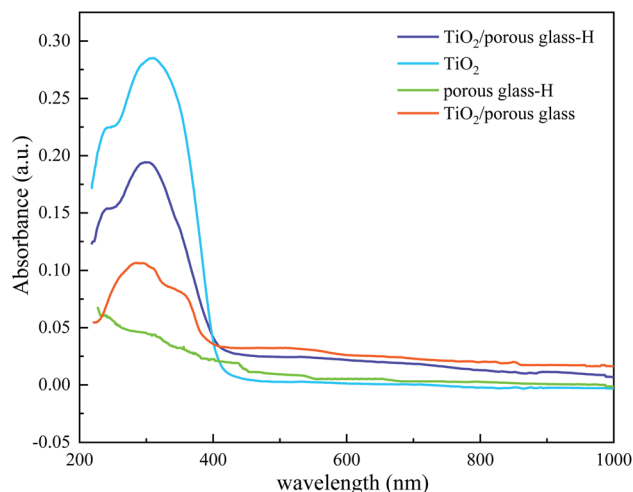

Fig. 3 UV-vis diffuse reflectance spectra of TiO_2-H, porous glass-H, TiO_2/porous glass and TiO_2/porous glass-H.

absorption limit can be roughly evaluated from the absorption edge value using the following equation:[42]

$$E_g = \frac{hc}{\lambda} = \frac{1240}{\lambda} (\text{eV}) \qquad (2)$$

where E_g, h, c and λ are the band gap energy (eV), Planck's constant (6.626×10^{-34} J s^{-1}), the velocity of light (3×10^8 m s^{-1}) and the absorption edge (nm), respectively. The calculated band gap for TiO$_2$/porous glass and TiO$_2$/porous glass-H is 4.32 eV and 4.01 eV, respectively. The narrower band gap of TiO$_2$/porous glass-H can cause the transition energy barrier of electrons to be overcome more easily, which can effectively improve the photocatalytic performance of the semiconductor photocatalyst. Therefore, it can be inferred that under the same conditions, the desulfurization rate of TiO$_2$/porous glass-H is higher than that of TiO$_2$/porous glass. To verify this conjecture, the two catalysts were subjected to photocatalytic oxidative desulfurization tests under ultraviolet light irradiation.

3.2 Linearity and sensitivity of the detection method

The concentration of the standard solution was taken as the abscissa (x) and the peak area of the spectrum is taken as the ordinate (y) to draw a standard curve. The linear regression equation is shown in Fig. 4. Under the above-mentioned mass spectrometry conditions, the concentration of the simulated oil standard solution (the DBT concentration is in the range of 10 mg L^{-1} to 900 mg L^{-1}) has a good linear relationship with its peak area ($R^2 \geq 0.99$).

The sensitivity of the test method is expressed by the detection limit and the quantification limit. The detection limit is defined as the concentration of the target when S/N = 3, and the limit of quantification is defined as the concentration when S/N = 10. Finally, the detection limit and quantification limit of this method were determined to be 2.18 mg L^{-1} and 7.26 mg L^{-1}, respectively.

3.3 Desulfurization performance of TiO$_2$/porous glass and TiO$_2$/porous glass-H

Fig. 5 shows the desulfurization performance of TiO$_2$/porous glass and TiO$_2$/porous glass-H with and without UV irradiation.
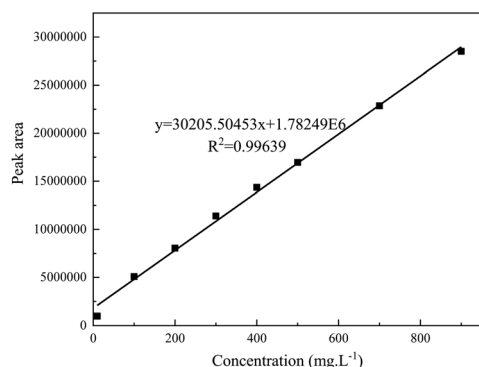

Fig. 4 Standard curve obtained with different concentrations of DBT.
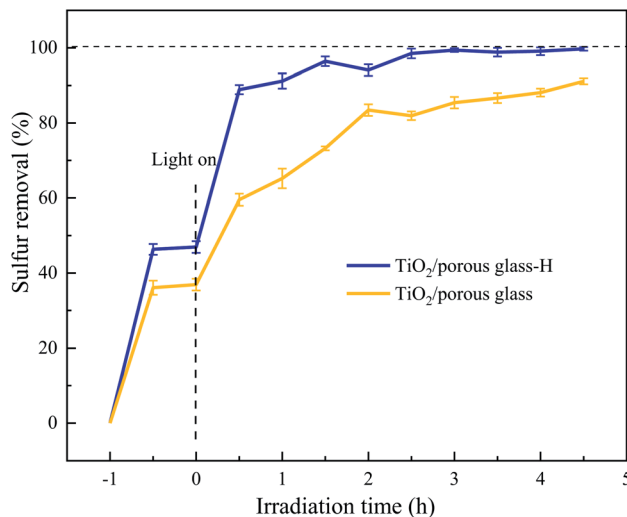

Fig. 5 Desulfurization performance of TiO$_2$/porous glass and TiO$_2$/porous glass-H with and without UV irradiation.

Before UV irradiation, the adsorption equilibrium of DBT on both materials was attained within 1 h. TiO$_2$/porous glass-H showed a higher equilibrium adsorption capacity in comparison with the TiO$_2$/porous glass, probably due to the higher surface area of TiO$_2$/porous glass-H, which is consistent with the results from the SEM and N$_2$ adsorption–desorption measurements. After UV irradiation, the sulfur removal distinctly increased for both catalysts. This phenomenon can be explained by the photocatalytic adsorption desulfurization mechanism, where organosulfur compounds are firstly photocatalytically oxidized to sulfoxides or sulfones through photocatalytic active components, which are then selectively adsorbed on the photocatalytic oxidation–adsorption bifunctional material due to the high polarity of the sulfoxides or sulfones produced.[43–45] TiO$_2$/porous glass-H showed a much higher photocatalytic oxidation–adsorption desulfurization efficiency than TiO$_2$/porous glass in a specific period. This is mainly because of the larger surface area and narrower band gap width of TiO$_2$/porous glass-H, resulting in a higher UV absorption capacity. In addition, a larger surface area allows the active sites to be more uniformly dispersed and photogenerated carrier recombination is more difficult, resulting in a higher desulfurization efficiency higher. With UV irradiation, TiO$_2$/porous glass-H further presented 40% removal of sulfur content within 30 min, which then gradually levelled off, approaching almost 100% sulfur removal. In contrast, TiO$_2$/porous glass took 1.5 h to further achieve 40% removal of sulfur content and approached only 90% sulfur removal within the testing period (4.5 h).

3.4 Influence of TiO$_2$ loading and reaction time on desulfurization performance

Fig. 6 shows the influence of the TiO$_2$ loading in TiO$_2$/porous glass-H on its desulfurization performance with and without UV irradiation. Before UV irradiation, TiO$_2$/porous glass-H (x =
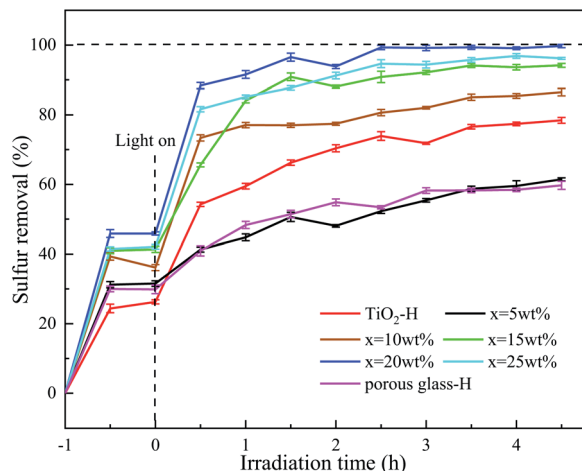
Fig. 6 Desulfurization performance of TiO₂/porous glass-H with different TiO₂ loadings.

20 wt%) showed the highest equilibrium adsorptive capacity for DBT. However, the surface area of TiO₂/porous glass-H ($x = 20$ wt%) was not the highest, as show in Table 1, indicating that the surface area was not the dominant factor affecting the adsorption capacity of TiO₂/porous glass-H. After UV irradiation, the sulfur removal rate showed an upward trend with an increase in the reaction time. It can be seen that the increase was extremely slow in the desulfurization rate when the reaction time exceeded 2.5 h. It can be inferred that the reaction reached a dynamic equilibrium state at this time. Among them, the removal rate of DBT significantly increased for the TiO₂-H single oxide, indicating that TiO₂ in TiO₂/porous glass-H not only acted as the photocatalytic active sites but was also the sulfide adsorption sites for sulfide. In contrast, the sulfur removal only slightly increased in the presence of porous glass-H, suggesting that the carrier of TiO₂/porous glass-H mainly served as the adsorptive sites rather than the active sites. For the various TiO₂/porous glass-H, the desulfurization rate of the model fuel increased with an increase in the TiO₂ loading up to

20 wt%, which was caused by the increase in the surface area, UV absorption and adsorption sites in the catalyst, and also more uniform distribution of the catalytic sites. The desulfurization rate of the model fuel then decreased when the TiO₂ loading was greater that 20 wt%, which can be ascribed to the decrease in surface area and increase in the crystalline size.

3.5 The effect of reaction temperature and sulfide concentration on desulfurization performance

The influence of concentration and reaction temperature of sulfide in the simulated oil on the desulfurization performance is plotted in Fig. 7 and 8, respectively. It can be seen that the desulfurization rate of the model fuel increased when the reaction temperature increased from 293.15 to 303.15 K. When the reaction temperature increased to 333.15 K, the desulfurization rate slightly decreased from 100% to 87%. However, it can be seen from Fig. 8 that the concentration of sulfide has a major impact on the desulfurization performance. When the concentration of sulfide increased from 200 to 300 mg L⁻¹, the desulfurization rate hardly changed. Then, the desulfurization rate suddenly decreased from nearly 100% to 67% when the concentration of sulfide increased to 400 mg L⁻¹. This may be because the adsorption capacity of the adsorption site was saturated when the sulfide concentration was 300 mg L⁻¹. In addition, it was occupied by adsorbates and no further catalytic reactions could occur due to the fact that TiO₂ not only serves as the catalytic sites but also as adsorption sites, resulting in a sharp decrease in the desulfurization rate.

3.6 Adsorption kinetics

According to the work of Nair[46] and Shen,[47] acid–base interactions and polar molecular interactions are also important factors affecting the adsorption capacity of catalysts. Therefore, it can be inferred that the excellent sulfide adsorption capacity of TiO₂/porous glass-H ($x = 20$ wt%) may result from the synergistic effect of physical adsorption caused by the van der
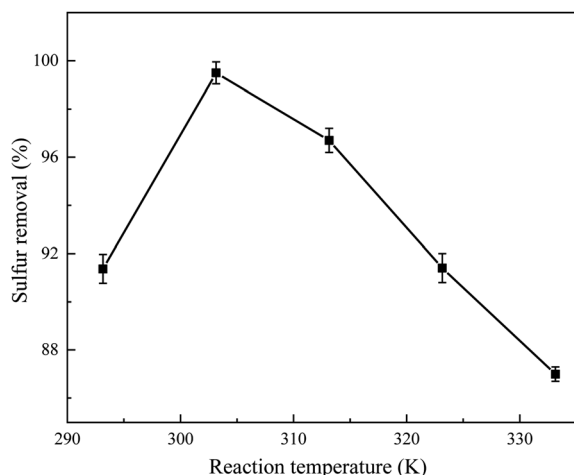

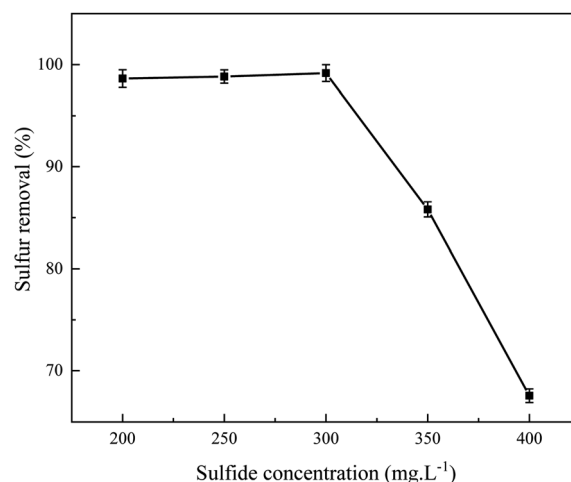**Fig. 7** Effect of reaction temperature on desulfurization performance.

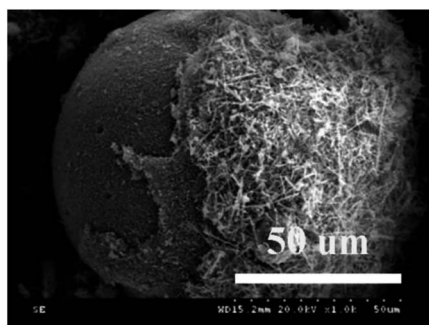**Fig. 8** Influence of sulfide concentration on desulfurization performance.

Fig. 9 SEM micrograph of TiO$_2$/porous glass-H with core–shell structure.

Fig. 11 Adsorption fitting curve of the internal diffusion model.

Waals interaction and acid–base interactions between the sulfur heterocycle and active center. This hypothesis can be verified by the adsorption kinetics. The adsorption process of sulfide mainly includes three stages as follows: (1) the diffusion of sulfide from the oil phase to the surface of the adsorbent, which is called membrane diffusion. (2) The diffusion of sulfide from the surface of the adsorbent along the pores of the adsorbent to the adsorption site, which is called internal diffusion. (3) Sulfide is adsorbed on the adsorption site of the adsorbent by physical adsorption. The extremely fast physical adsorption rate in the third step has little effect on the adsorption rate.

As shown in Fig. 9, considering that the porous glass beads used in this work possess a core–shell structure, leading to a short diffusion length for the carrier, the influence of internal diffusion on the overall adsorption rate in the second step was weakened. To determine the decisive steps in the entire adsorption process, the membrane diffusion model and the intraparticle diffusion model were used to fit the kinetic data. The linear expression of the film diffusion model is expressed as eqn (3).[48,49]

$$\begin{cases} \ln(1 - F) = -kt \\ F = q_t/q_{et} \end{cases} \quad (3)$$
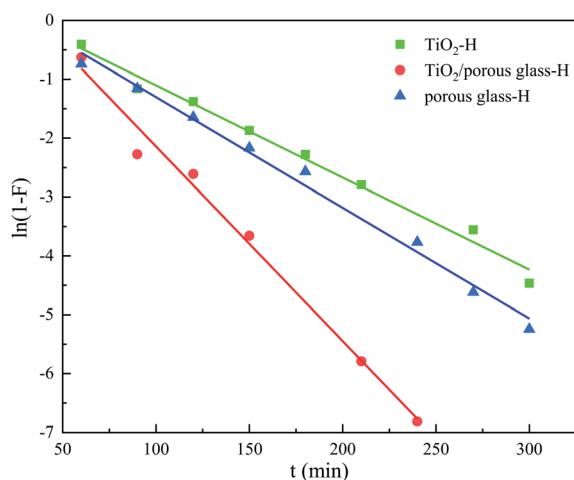
where k is the adsorption rate constant, F is a balanced realization index, t is the time when the catalyst is added to the fuel, q_t is the adsorption amount at time t and q_{et} is the adsorption amount after reaching equilibrium.

The linear expression of the intraparticle diffusion model is expressed as eqn (4).[48,49]

$$q_t = k \times t^{0.5} \quad (4)$$

where k and q_t are the same as the previous definitions and k is the rate constant, with the units of mg $(g^{-1} min^{-0.5})$.

Fig. 10 shows the result of the adsorption kinetics fitting of the three samples according to the film diffusion model, and Fig. 11 shows the fitting result of the intraparticle diffusion model. The related parameters are listed in Table 2. The correlation shows that the sorption data is better represented by the film diffusion model, that is, the rate-controlling step of the adsorption of sulfide on the catalyst is the molecular diffusion process. Intraparticle diffusion was not the rate-determining step of the sulfide adsorption process, but it will influence the sorption process.

3.7 Adsorption thermodynamics

To verify the effectiveness of the photocatalytic oxidation–adsorption system, the adsorption isotherms of DBT over TiO$_2$/porous glass-H and porous glass-H were compared, as shown in

Fig. 10 Adsorption fitting curve of the film diffusion model.

Table 2 The fitted data and correlation coefficient between the membrane diffusion model and the intraparticle diffusion model

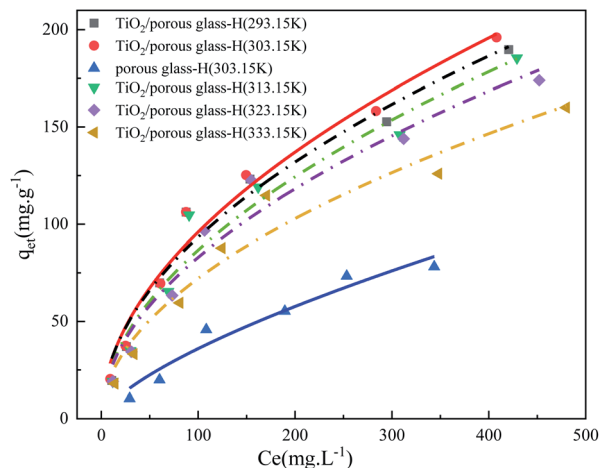| Sample name | Film diffusion model | | Intraparticle diffusion model | |
	k min	R^2	k (mg g^{-1} min$^{-0.5}$)	R^2
TiO$_2$-H	0.0157	0.9875	7.2442	0.8920
TiO$_2$/porous glass-H	0.0331	0.9884	7.1038	0.7314
Porous glass-H	0.0188	0.9907	4.1568	0.9325

Fig. 12 Fitting curves of the adsorption thermodynamics using the Freundlich model.

Fig. 12. The adsorption thermodynamic behavior of the different catalysts on DBT was investigated at a temperature in the range of 293.15 to 333.15 K, and the Freundlich model was selected for fitting. The expression is described in eqn (5) and the relevant parameters are listed in Table 3.[50,51]

$$q_{et} = K_F \times C_e^{1/n} \qquad (5)$$

where C_e is the concentration of DBT in the liquid phase at equilibrium, the unit is mg L^{-1}; q_{et} is the adsorption capacity of the adsorbent after the adsorption reaches equilibrium, with the units of mg g^{-1}; K_F is the Freundlich constant, with the units of (mg g^{-1})/(mg L^{-1})$^{1/n}$; and n(dimensionless) is the Freundlich parameter, which indicates the magnitude of the adsorption driving force or the surface heterogeneity.

The high R^2 (>0.95) suggests that both the composite catalyst and carrier isotherm can be well presented by the Freundlich adsorption model. The Freundlich parameter n is used to evaluate the adsorption intensity of the adsorption reaction.[52,53] It is favorable for adsorption when the value of $1/n$ is between 0 and 1, and it is unfavorable adsorption when the value of $1/n$ is greater than 2. In addition, it is generally believed that where the value of $1/n$ is closer to 0.1, and the adsorption performance is better. The inverse of the Freundlich parameter $1/n$ of TiO$_2$/porous glass-H is smaller than that of porous glass-H, suggesting that the adsorption capacity was significantly enhanced for TiO$_2$/porous glass-H when titanium dioxide was introduced in porous glass-H. Conversely, K_F of TiO$_2$/porous glass-H was as high as 8.9645 (mg g^{-1})/(mg L^{-1})$^{1/n}$, which is around 5.8 times that of porous glass-H. This shows that the adsorption driving force was enhanced due to the fact that the density of sulfur adsorption sites also increased after TiO$_2$ loading. As previously mentioned, the origin of the adsorption sites on TiO$_2$/porous glass-H and porous glass-H is different. Porous glass-H adsorbs sulfide through the interaction between polar molecules, while for TiO$_2$/porous glass-H, TiO$_2$ is not only considered as the catalytic sites but also the adsorption sites through the interaction of its Bronsted acid centers and the mutual cooperation of polar molecules with DBT.[46,54]

According to the work of Ghosal[55] and Tran,[56] the equilibrium constant K_c derived from the Freundlich constant can be described as eqn (6)

$$K_c = \frac{K_F \rho}{1000} \left(\frac{10^6}{\rho}\right)^{\left(1 - \frac{1}{n}\right)} \qquad (6)$$

where ρ is the density of pure water (assumed as ~1.0 g mL^{-1}). The values of the parameters ΔG, ΔH, and ΔS can be calculated using eqn (7) and (8).

Table 3 Freundlich model fitting data and correlation coefficient

Sample name	Temperature (K)	Freundlich model			
		K_F (mg g^{-1})/(mg L^{-1})$^{1/n}$	$1/n$	n	R^2
TiO$_2$/porous glass-H	293.15	9.3449	0.5151	1.9414	0.9687
TiO$_2$/porous glass-H	303.15	8.9645	0.5147	1.9429	0.9777
Porous glass-H	303.15	1.5572	0.6817	1.4669	0.9534
TiO$_2$/porous glass-H	313.15	8.4636	0.5168	1.9349	0.9578
TiO$_2$/porous glass-H	323.15	7.8668	0.5114	1.9555	0.9605
TiO$_2$/porous glass-H	333.15	6.8341	0.5086	1.9662	0.9546

Table 4 Thermodynamic parameters of dibenzothiophene adsorbed by TiO$_2$/porous glass-H

T/(K)	K_F/((mg g^{-1})/(mg L^{-1})$^{1/n}$)	$1/n$	K_c	ΔG/(kJ mol^{-1})	ΔH/(kJ mol^{-1})	ΔS/(J mol^{-1} K^{-1})	R^2
293.15	9.3449	0.5151	6.3123	−4.49	−4.25	0.88	0.9282
303.15	8.9645	0.5147	6.0897	−4.55			
313.15	8.4636	0.5168	5.5809	−4.48			
323.15	7.8668	0.5181	5.5999	−4.63			
333.15	6.8341	0.5114	5.0617	−4.49			

$$\Delta G = -RT \ln\left(\frac{K_F \rho}{1000}\left(\frac{10^6}{\rho}\right)^{\left(1-\frac{1}{n}\right)}\right) \qquad (7)$$

$$\ln\left(\left(\frac{K_F \rho}{1000}\right)\left(\frac{10^6}{\rho}\right)^{\left(1-\frac{1}{n}\right)}\right) = \frac{-\Delta H}{R} \times \frac{1}{T} + \frac{\Delta S}{R} \qquad (8)$$

When the calculation method of Ghosa and Tran is applied to this experiment, ρ is the density of pure n-octane (assumed to be $\sim$0.7 g mL^{-1}); the unit of K_F is (mg g^{-1})/(mg L^{-1})$^{1/n}$; K_c is the equilibrium constant at different temperatures; R is the universal gas constant (8.3144 J (mol^{-1} K^{-1})) and T is the absolute temperature in Kelvin. The calculated thermodynamic parameters are shown in Table 4.

The curve fitted by the equation $\ln K_c = \frac{-\Delta H}{R} \times \frac{1}{T} + \frac{\Delta S}{R}$ and the corresponding coefficients are shown in Fig. 13.

3.8 Regeneration

The regeneration of TiO$_2$/porous glass-H was conducted by thermal treatment in air. Fig. 14 presents the recycling performance of TiO$_2$/porous glass-H in a series of three consecutive desulfurization–regeneration cycles. It is obvious that the performance of the regenerated TiO$_2$/porous glass-H is repeatable and comparable to that of the original TiO$_2$/porous glass-H. Compared with other studies using acetonitrile to extract sulfide,[57,58] the heat treatment method for TiO$_2$/porous glass-H can effectively avoid the use of toxic materials, which can be a very promising method for industrial applications with reduced cost and increased recyclability.

3.9 Desulfurization mechanism of TiO$_2$/porous glass-H catalyst

To further explore the removal mechanism of the target sulfide, radical trapping experiments using different scavengers of p-benzoquinone (BQ), iso-propyl alcohol (IPA), and edetate disodium (EDTA-Na2) were implemented to determine the relative roles of the reactive species superoxide radicals ($^{\bullet}O_2^{-}$), hydroxyl
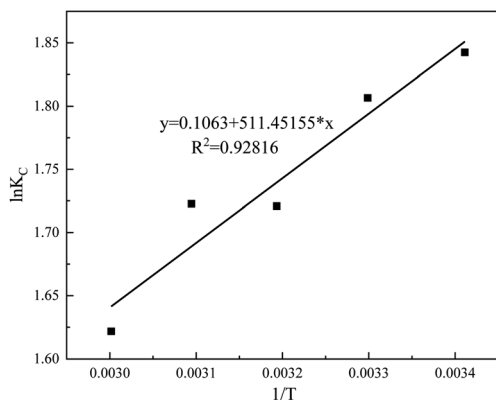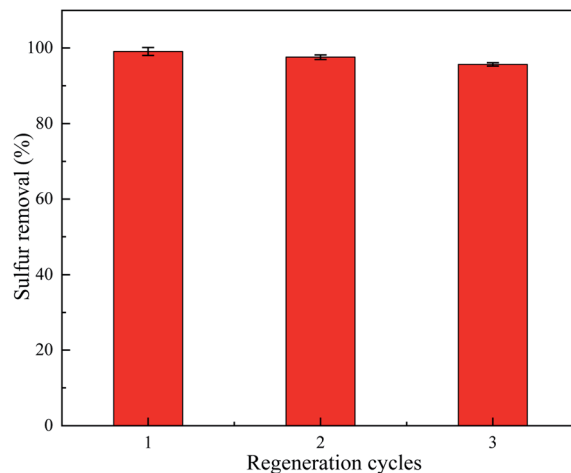

Fig. 14 Recycling performance of TiO$_2$/porous glass-H.

radicals ($^{\bullet}$OH) and h^{+}, respectively. The test results are shown in Fig. 15.

It can be observed from Fig. 15 that the desulfurization performance of DBT on the TiO$_2$/porous glass-H catalyst with scavengers of BQ and EDTA-Na2 was lower compared with the catalyst without scavengers. However, the desulfurization rate of DBT on the TiO$_2$/porous glass-H catalyst with the IPA scavenger had the maximum reduction, which shows that $^{\bullet}$OH plays the most important role in the removal process of DBT among the free radicals. Therefore, it can be inferred that the uniformly distributed TiO$_2$ on the porous glass underwent the process shown in Fig. 16 upon exposure to ultraviolet light irradiation. Firstly, the sulfide in the oil is adsorbed on the surface of the catalyst under the effect of polarity. Subsequently, the photocatalytic oxidation reaction process of DBT occurring on the catalytic site is considered to be the following: electrons are excited firstly from the valence band to the conduction band to generate electron–hole pairs over TiO$_2$ in TiO$_2$/porous glass-H under ultraviolet light irradiation. Electrons interact with an oxygen molecule to form $^{\bullet}O_2^{-}$, which can further form $^{\bullet}$OH. Simultaneously, the holes interact with water molecules to form

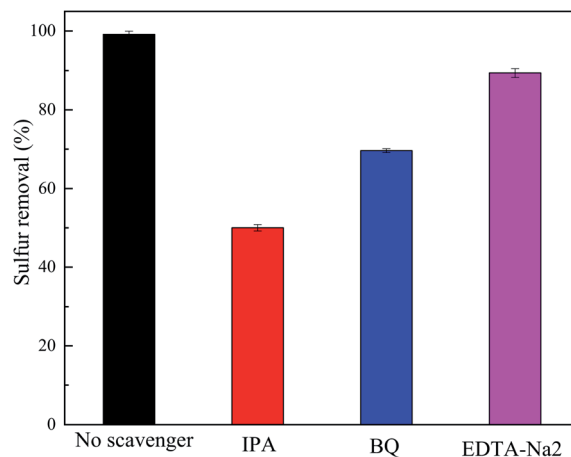Fig. 13 Fitting curve of $\ln K_c$ and $1/T$.

y=0.1063+511.45155*x
R^2=0.92816

Fig. 15 Radical trapping experiment of TiO$_2$/porous glass-H to remove DBT under simulation.

Fig. 16 Desulfurization mechanism of TiO$_2$/porous glass-H.

$^{\bullet}$OH. Subsequently, DBT is oxidized by $^{\bullet}$O$_2^{-}$ and $^{\bullet}$OH to sulfones and sulfoxides, and then the generated polar sulfoxides and sulfones are selectively adsorbed on the adsorption sites of the porous glass or TiO$_2$ in TiO$_2$/porous glass-H to achieve the coupling of photocatalysis oxidation–adsorption in the initial position. The porous glass carrier with abundant pores and core–shell structure and the inhibition of the hydrolysis process in the presence of H$_2$O$_2$ are responsible for the morphology control of TiO$_2$/porous glass-H, and core–shell structure is formed with a large specific surface area, narrow particle size distribution and uniform dispersion. The core–shell structure with a large specific surface area not only increases the reaction contact area and light absorption capacity between the catalyst and fuel, but also accelerates the mass transfer of sulfide through physical adsorption, and further enhances the desulfurization performance of the photocatalytic oxidation–adsorption in the initial position coupling system. In addition, no additional oxidants (such as H$_2$O$_2$ and O$_3$) are introduced in the desulfurization system coupled by photocatalytic oxidation–adsorption in the initial position. Thus, the above-mentioned method not only solves the problem of low mass transfer efficiency caused by the extreme polarity ratio of oil to oxidant compared with the desulfurization method of adding oxidants, but also makes the operation safer and reduces the post-processing steps.

4 Conclusion

Coupling of a photocatalysis oxidation–adsorption system for model diesel fuel using TiO$_2$/porous glass-H composite catalysts under mild conditions was developed in this work. The structure and morphology of the composite catalysts were characterized and the influence of various factors on their desulfurization efficiency was investigated. The results showed that the use of H$_2$O$_2$ to assist the synthesis of the composite catalysts effectively promoted the uniform distribution of TiO$_2$ on the carrier, resulting in an increase in the surface area of the catalyst and improving the efficiency of photocatalytic oxidation. Moreover, the surface area of the catalyst carriers was not the main factor affecting the desulfurization rate, but the balance between the catalytic site and the adsorption site was the decisive factor in improving the desulfurization efficiency. The rate-controlling step of sulfide on the catalyst was a molecular diffusion process, where the adsorption intensity and adsorption capacity of the composite catalyst significantly improved compared with porous glass-H. Also, it was concluded that the photocatalytic oxidation–adsorption process can proceed spontaneously based on the calculated ΔS, ΔH and ΔG values. In addition, the composite catalyst adsorbed sulfide through van der Waals force and acid–base interactions, enabling a green heat treatment method to regenerate the composite catalyst, which exhibited similar efficiency as the original composite catalyst after three regeneration cycles. Finally, the reaction mechanism of the coupling system of photocatalytic oxidation reaction and adsorption separation in the initial position was proposed, which provides a novel route for green and low-cost desulfurization.

Conflicts of interest

There are no conflicts to declare.

Acknowledgements

© 2021 The Author(s). Published by the Royal Society of Chemistry

References

1 A. H. M. Shahadat Hussain and B. J. Tatarchuk, Mechanism of hydrocarbon fuel desulfurization using Ag/TiO$_2$–Al$_2$O$_3$ adsorbent, *Fuel Process. Technol.*, 2014, **126**, 233–242.

2 M. H. Ibrahim, M. Hayyan, M. A. Hashim, *et al.*, The role of ionic liquids in desulfurization of fuels: a review, *Renewable Sustainable Energy Rev.*, 2017, **76**(9), 1534–1549.

3 R. Dehghan and M. Anbia, Zeolites for adsorptive desulfurization from fuels: a review, *Fuel Process. Technol.*, 2017, **167**, 99–116.

4 R. Abro, A. A. Abdeltawab, S. S. Al-Deyab, *et al.*, A review of extractive desulfurization of fuel oils using ionic liquids, *RSC Adv.*, 2014, **4**(67), 35302–35317.

5 Y. S. AI-Degs, A. H. EI-Sheikh, R. Z. Al-Bakain, *et al.*, Conventional and upcoming sulfur-cleaning technologies for petroleum fuel: a review, *Energy Technol.*, 2016, **4**(6), 679–699.

6 A. Tanimu and K. Alhooshani, Advanced hydrodesulfurization catalysts: a review of design and synthesis, *Energy Fuels*, 2019, **33**(4), 2810–2838.

7 A. Lopez-Benitez, G. Berhault and A. Guevara-Lara, NiMo catalysts supported on Mn–Al$_2$O$_3$ for dibenzothiophene hydrodesulfurization application, *Appl. Catal., B*, 2017, **213**, 28–41.

8 L. L. Zhang, X. Chen and C. H. Liang, Improving Hydrodesulfurization Performance of Sulfur resistant Intermetallic Ni$_2$Si Based on MOF-derived Route, *Inorg. Chem. Front.*, 2020, **8**(5), 1–6.

9 Q. Wang, T. Zhang, S. L. Zhang, *et al.*, Extractive desulfurization of fuels using trialkylamine-based protic ionic liquids, *Sep. Purif. Technol.*, 2020, **231**, 115923–115929.

10 X. Liu, J. Y. Wang, Q. Y. Li, *et al.*, Synthesis of rare earth metal–organic frameworks (Ln–MOFs) and their properties of adsorption desulfurization, *J. Rare Earths*, 2014, **32**(2), 189–194.

11 L. C. Song, Z. B. Duan, L. J. Zhu, *et al.*, Selective functionalization of external and internal surface of MCM-41 for adsorptive desulfurization, *J. Porous Mater.*, 2016, **23**(5), 1181–1187.

12 M. Ja'fari, S. L. Ebrahimi and M. R. Khosravi-Nikou, Ultrasound-assisted oxidative desulfurization and denitrogenation of liquid hydrocarbon fuels: a critical review, *Ultrason. Sonochem.*, 2018, **40**(9), 955–968.

13 H. Shang, H. C. Zhang, W. Du, *et al.*, Development of microwave assisted oxidative desulfurization of petroleum oils: a review, *J. Ind. Eng. Chem.*, 2013, **19**(5), 1426–1432.

14 A. E. S. Choi, S. Roces, N. Dugos, *et al.*, Oxidation by H$_2$O$_2$ of benzothiophene and dibenzothiophene over different polyoxometalate catalysts in the frame of ultrasound and mixing assisted oxidative desulfurization, *Fuel*, 2016, **180**(15), 127–136.

15 G. Mohebali and A. S. Ball, Biocatalytic desulfurization (BDS) of petrodiesel fuels, *Microbiology*, 2008, **154**(8), 2169–2183.

16 A. A. Nuhu, Bio-catalytic desulfurization of fossil fuels: a mini review, *Rev. Environ. Sci. Bio/Technol.*, 2013, **12**(1), 9–23.

17 M. M. A. Alhussaini and N. S. Ahmedzeki, Reactive Adsorption Desulfurization by Nanocrystalline ZnO/Zeolite A Molecular Sieves, *Journal of Web Engineering*, 2017, **23**(9), 38–49.

18 H. Z. Li, L. X. Dong, L. Zhao, *et al.*, Enhanced Adsorption Desulfurization Performance over Mesoporous ZSM-5 by Alkali Treatment, *Ind. Eng. Chem. Res.*, 2017, **56**(14), 3813–3821.

19 M. X. Tang, W. X. Wang, L. G. Zhou, *et al.*, Reactive adsorption desulfurization of thiophene over NiMo/ZnO, a new adsorbent with high desulfurization performance and sulfur capacity at moderate temperature, *Catal. Sci. Technol.*, 2019, **9**(22), 6318–6326.

20 J. L. Cheng, S. L. Jin, R. Zhang, *et al.*, Enhanced adsorption selectivity of dibenzothiophene on ordered mesoporous carbon–silica nanocomposites *via* copper modification, *Microporous Mesoporous Mater.*, 2015, **212**, 137–145.

21 S. Velu, X. L. Ma, C. S. Song, *et al.*, Selective Adsorption for Removing Sulfur from Jet Fuel over Zeolite-Based Adsorbents, *Ind. Eng. Chem. Res.*, 2003, **42**(21), 5293–5304.

22 M. Q. Zheng, H. Hu, Z. L. Ye, *et al.*, Adsorption desulfurization performance and adsorption-diffusion study of B$_2$O$_3$ modified Ag–CeO$_x$/TiO$_2$–SiO$_2$, *J. Hazard. Mater.*, 2019, **362**, 424–435.

23 Y. Q. Liu, H. Y. Wang, J. C. Zhao, *et al.*, Ultra-deep desulfurization by reactive adsorption desulfurization on copper-based catalysts, *J. Energy Chem.*, 2019, **29**, 8–16.

24 X. Q. Lin, X. Y. Zeng, R. J. Zhou, *et al.*, Unified catalytic oxidation–adsorption desulfurization for aromatic sulfur compounds with cyclohexanone peroxide over Ti-HMS, *React. Kinet., Mech. Catal.*, 2019, **126**(1), 353–364.

25 S. G. Kumar and L. G. Devi, Review on modified TiO$_2$ photocatalysis under UV/visible light: selected results and related mechanisms on interfacial charge carrier transfer dynamics, *J. Phys. Chem. A*, 2011, **115**(46), 13211–13241.

26 G. Q. Guo, H. Y. Guo, F. Wang, *et al.*, Dye-sensitized TiO$_2$@SBA-15 composites: preparation and their application in photocatalytic desulfurization, *Green Energy Environ.*, 2020, **5**(1), 114–120.

27 B. Amin, A. K. Abbas, H. M. Alireza, *et al.*, Microporous titania–silica nanocomposite catalyst-adsorbent for ultra-deep oxidative desulfurization, *Appl. Catal., B*, 2016, **180**, 65–77.

28 X. L. Ren, G. Miao, Z. Y. Xiao, *et al.*, Catalytic adsorptive desulfurization of model diesel fuel using TiO$_2$/SBA-15 under mild conditions, *Fuel*, 2016, **174**(15), 118–125.

29 X. Li, Y. L. Xu, C. Zhang, *et al.*, H$_2$O$_2$-assisted hydrothermal synthesis of TiO$_2$–SiO$_2$ and its enhanced photocatalytic-adsorptive desulfurization performance for model fuel, *Fuel*, 2018, **226**(15), 527–535.

30 G. Miao, F. Y. Ye, L. M. Wu, et al., Selective adsorption of thiophenic compounds from fuel over TiO$_2$/SiO$_2$ under UV-irradiation, J. Hazard. Mater., 2015, 300(30), 426–432.

31 B. L. Jiang, N. Jiang and Y. X. Chang, Synthesis of highly active Cu(ɪ)-Y(ɪɪɪ)-Y zeolite and its selective adsorption desulfurization performance in presence of xylene isomers, Pet. Sci., 2021, 18(1), 295–306.

32 J. H. Kim, X. Ma, A. Zhou, et al., Ultra-deep desulfurization and denitrogenation of diesel fuel by selective adsorption over three different adsorbents: a study on adsorptive selectivity and mechanism, Catal. Today, 2006, 111(1–2), 74–83.

33 Z. Q. Li, Y. Zhu, L. W. Wang, et al., A facile method for the structure control of TiO$_2$ particles at low temperature, Appl. Surf. Sci., 2015, 355(15), 1051–1056.

34 Z. G. Sun, X. S. Li, X. B. Zhu, et al., Facile and Fast Deposition of Amorphous TiO$_2$ Film under Atmospheric Pressure and at Room Temperature, and its High Photocatalytic Activity under UV-C Light, Chem. Vap. Deposition, 2013, 20, 8–13.

35 J. Q. Zhuang, G. Yang, D. Ma, et al., In Situ Magnetic Resonance Investigation of Styrene Oxidation over TS-1 Zeolites, Angew. Chem., 2004, 43(46), 6377–6381.

36 P. Wu, T. Tatsumi, T. Komatsu, et al., A Novel Titanosilicate with MWW Structure: II. Catalytic Properties in the Selective Oxidation of Alkenes, J. Catal., 2001, 202(2), 245–255.

37 H. Yin, Y. Wada, T. Kitamura, et al., Hydrothermal synthesis of nanosized anatase and rutile TiO$_2$ using amorphous phase TiO$_2$, J. Mater. Chem., 2001, 11(6), 1694–1703.

38 M. L. Han, Z. Q. Dong, J. A. Liu, et al., The role of lanthanum in improving the visible-light photocatalytic activity of TiO$_2$ nanoparticles prepared by hydrothermal method, Appl. Phys. A: Mater. Sci. Process., 2020, 126(12), 1–10.

39 D. S. Kim and S. Y. Kwak, The hydrothermal synthesis of mesoporous TiO$_2$ with high crystallinity, thermal stability, large surface area, and enhanced photocatalytic activity, Appl. Catal., A, 2007, 323, 110–118.

40 C. L. Pang, R. Lindsay and G. Thornton, Structure of Clean and Adsorbate-Covered Single-Crystal Rutile TiO$_2$ Surfaces, Chem. Rev., 2013, 113(6), 3887–3948.

41 D. Arun Kumar, J. Merline Shyla and F. P. Xavier, Synthesis and characterization of TiO$_2$/SiO$_2$ nano composites for solar cell applications, Appl. Nanosci., 2012, 2(4), 429–436.

42 S. A. Ansari, M. M. Khan, M. O. Ansari, et al., Gold nanoparticles-sensitized wide and narrow band gap TiO$_2$ for visible light applications: a comparative study, New J. Chem., 2015, 39(6), 4708–4715.

43 H. H. Andevary, A. Akbari and M. Omidkhah, High efficient and selective oxidative desulfurization of diesel fuel using dual-function FeCl$_4$ as catalyst/extractant, Fuel Process. Technol., 2019, 185, 8–17.

44 X. J. Mei, J. Bai, S. Chen, et al., Efficient SO$_2$ removal and highly synergistic H$_2$O$_2$ production based a novel dual-function photoelectrocatalytic system, Environ. Sci. Technol., 2020, 54(18), 11515–11525.

45 S. Y. Dou and R. Wang, Study on the performance and mechanism of aerobic oxidative desulfurization based on a dual-functional material possessing catalytic and adsorptive properties, New J. Chem., 2019, 43(7), 3226–3235.

46 S. Nair, A. H. M. S. Hussain and B. J. Tatarchuk, The role of surface acidity in adsorption of aromatic sulfur heterocycles from fuels – ScienceDirect, Fuel, 2013, 105(2), 695–704.

47 C. Shen, Y. J. Wang, J. H. Xu, et al., Oxidative desulfurization of DBT with H$_2$O$_2$ catalysed by TiO$_2$/porous glass, Green Chem., 2016, 18(3), 771–781.

48 C. Shen, Y. J. Wang, J. H. Xu, et al., Preparation and ion exchange properties of egg-shell glass beads with different surface morphologies, Particuology, 2012, 10(3), 317–326.

49 P. Nugent, Y. Belmabkhout, S. D. Burd, et al., Porous materials with optimal adsorption thermodynamics and kinetics for CO$_2$ separation, Nature, 2013, 495(7439), 80–84.

50 M. Naushad, Z. A. Alothman, G. Sharma, et al., Kinetics, isotherm and thermodynamic investigations for the adsorption of Co(ɪɪ) ion onto crystal violet modified Amberlite IR-120 resin, Ionics, 2015, 21(5), 1453–1459.

51 N. T. Hai, S. J. You, A. Hosseini-Bandegharaei, et al., Mistakes and inconsistencies regarding adsorption of contaminants from aqueous solutions: a critical review, Water Res., 2017, 120(1), 88–116.

52 E. Elgueta, B. L. Rivas, A. Mancisidor, et al., Hydrogels derived from 2-hydroxyethyl-methacrylate and 2-acrylamido-2-methyl-1-propanesulfonic acid, with ability to remove metal cations from wastewater, Polym. Bull., 2019, 79(12), 6503–6528.

53 R. Katal, M. S. Baei, H. T. Rahmati, et al., Kinetic, isotherm and thermodynamic study of nitrate adsorption from aqueous solution using modified rice husk, J. Ind. Eng. Chem., 2012, 18(1), 295–302.

54 S. Nair and B. J. Tatarchuk, Characteristics of sulfur removal by silver-titania adsorbents at ambient conditions, Adsorption, 2011, 17(4), 663–673.

55 P. S. Ghosal and A. K. Gupta, An insight into thermodynamics of adsorptive removal of fluoride by calcined Ca-Al-(NO$_3$) layered double hydroxide, RSC Adv., 2015, 5(128), 105889–105900.

56 H. N. Tran, S. J. You and H. P. Chao, Thermodynamic parameters of cadmium adsorption onto orange peel calculated from various methods: a comparison study, J. Environ. Chem. Eng., 2016, 4(3), 2671–2682.

57 A. Aghaei, S. Shahhosseini and M. A. Sobati, Regeneration of different extractive solvents for the oxidative desulfurization process: an experimental investigation, Process Saf. Environ. Prot., 2020, 139, 191–200.

58 D. Julião, F. Mirante, S. Ribeiro, et al., Deep oxidative desulfurization of diesel fuels using homogeneous and SBA-15-supported peroxo phosphotungstate catalysts, Fuel, 2019, 241, 616–624.